Nano Research

Open Access

Research Article

Silicalite-1 zeolite encapsulated Pt nanoparticles via ligand-protected *in-situ* construction for boosting auto-exhaust carbon particle oxidation

Yuanfeng Li[1,§], Tian Qin[3,§], Hao Guo[1], Yuechang Wei[1]✉, Yaxiao Ma[1], Linsheng Xu[1], Baolong Cui[1], Jing Xiong[1], Peng Zhang[1], Xi Liu[2,3]✉, Liwei Chen[3], Yunpeng Liu[4]✉, Jian Liu[1], and Zhen Zhao[1]

[1] *State Key Laboratory of Heavy Oil Processing, Key Laboratory of Optical Detection Technology for Oil and Gas, College of Science, China University of Petroleum, Beijing 102249, China*
[2] *School of Chemistry and Chemical Engineering, Ningxia University, Yinchuan 750021, China*
[3] *School of Chemistry and Chemical, In-situ Center for Physical Science, Frontiers Science Centre for Transformative Molecules, Shanghai Jiao Tong University, Shanghai 200240, China*
[4] *Multi-discipline Research Center, Institute of High Energy Physics, Chinese Academy of Sciences, Beijing 100049, China*
§ *Yuanfeng Li and Tian Qin contributed equally to this work.*

Cite this article: *Nano Research*, **2025**, *18*, 94907431. https://doi.org/10.26599/NR.2025.94907431

ABSTRACT: The enhancement of activity and stability of noble metal-based catalysts for purification of auto-exhaust carbon particle (soot) oxidation remains a grand challenge under harsh reaction conditions. Herein, the encapsulated catalysts of platinum nanoparticles (NPs) confined in silicalite-1 (S-1) zeolite were prepared by the ligand-protected *in-situ* synthesis method. The Pt NPs (4 nm) are located within the intersectional channels between the straight and the sinusoidal 10-ring channels of rigid S-1 zeolite and well stabilize inside the S-1 via Pt–O–Si bonds. The Pt@S-1 catalyst (0.38 wt.% of Pt loading) exhibits excellent performance (T_{50} = 368 °C, T_{50} corresponds to the temperatures at which 50% of soot conversion occurs) compared with the conventional Pt/S-1 catalyst during soot oxidation. The Pt@S-1 catalyst displays high long-term catalytic stability after the hydrothermal aging at 800 °C for 10 h, and the deactivation rate of the Pt@S-1 catalyst is one-tenth that of the Pt/S-1 catalyst. *In-situ* diffuse reflectance infrared Fourier transform spectroscopy (DRIFTS) and density functional theory (DFT) calculations corroborated that the encapsulated Pt NPs in Pt@S-1 catalyst display a higher *d*-band center than the isolated Pt NPs, which enhances bonding strength for co-adsorption of NO and O_2 molecules. The steric hindrance effect promotes the desorption of the critical intermediate of NO_2, which is the key step to the NO_2-assistant catalytic mechanism for soot oxidation. The ligand-protected *in-situ* confinement synthesis of metal nanoparticle catalysts not only ensures high activity and stability but also paves the way for the development of effective catalysts for soot oxidation in practical applications.

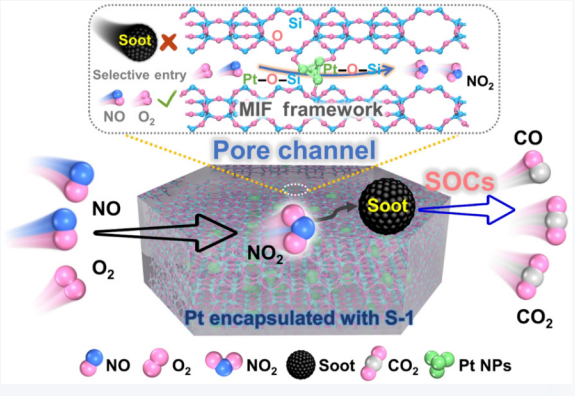

KEYWORDS: soot oxidation, silicalite-1, platinum nanoparticles, encapsulation, active oxygen species

1 Introduction

Engine exhaust releases carbon particles (soot) with adsorbed toxic substances, serving as the main contributor to PM 2.5 in urban environments. This pollution severely contaminates the atmosphere and poses significant risks to human health [1]. The catalytic after-treatment technique, composed of catalysts and a diesel particle filter (CDPF), is one of the most effective technique for reducing soot emissions [2, 3]. It relies on the design of efficient, economical, and environmentally friendly catalysts capable of promoting soot oxidation within the temperature window of exhaust gas from engines [4]. Researchers have extensively explored numerous efficient catalysts for soot oxidation, including noble metals, non-precious metal oxides (such as transition and alkali metals), and

Received: February 18, 2025; **Revised:** March 31, 2025
Accepted: April 2, 2025

✉Address correspondence to Yuechang Wei, weiyc@cup.edu.cn; Xi Liu, liuxi@sjtu.edu.cn; Yunpeng Liu, liuyunpeng@ihep.ac.cn

rare earth oxides [5–7]. Noble metal catalysts demonstrate outstanding catalytic efficiency, facilitating the oxidation of soot particles at relatively low temperatures [8, 9]. Platinum (Pt) catalysts have been widely applied in oxidation reactions, and they have always been the focus of attention. The presence of support can improve the dispersion of active sites, thereby increasing the utilization of noble metals and boosting the oxidation efficiency of catalysts [10]. Several types of support materials have been employed in soot oxidation, including active metal oxides (CeO_2, Co_3O_4, Mn_2O_3, and MnO_2) and inert Fe_2O_3, SiO_2, Al_2O_3, and zeolites [11–15]. However, these catalysts are prone to sintering and deactivation in high-temperature and humid environments, making it challenging to design Pt-based catalysts with both high activity and excellent stability for soot oxidation. Consequently, developing Pt-based catalysts that combine high activity with exceptional stability remains a significant challenge for efficient soot oxidation.

Catalytic soot oxidation is a characteristic heterogeneous deep oxidation process that takes place at the interface where catalysts, soot particles, and gas reactants (O_2 and NO) come into contact [16, 17]. To enhance the performance of catalysts for soot oxidation, two critical factors must be addressed: the contact efficiency between soot and the catalyst and the intrinsic activity for activating the reactants. Catalysts featuring porous structures can greatly enhance the contact efficiency between soot particles and the catalyst [18]. Zeolite materials have recently gained widespread use in the field of catalysis as supports due to their well-defined channels, along with their exceptional thermal and chemical stability, which facilitates the anchoring of active metal nanoparticles (NPs) [19–21]. Silicalite-1 (S-1) zeolite, with an MFI framework, is a purely siliceous material featuring a rich channel structure. It has a straight channel (5.3 Å × 5.6 Å) along the *b*-axis and zigzag channels (5.1 Å × 5.5 Å) along the *a*-axis [22]. Nevertheless, the size of soot particles exceeds the pore size of S-1, preventing effective interaction with the catalyst. Fortunately, the reactant molecules can freely pass through the pore channels, and the formation of intermediate NO_2 species can swiftly migrate to the soot surface [23]. It is widely recognized that soot oxidation occurs via an indirect pathway, where NO in the exhaust gas is first catalyzed by oxidation to form NO_2, which then oxidizes soot particles to CO_2 [24, 25]. Studies have shown that zeolite-supported noble metal catalysts have been effectively utilized for soot oxidation, exhibiting remarkable catalytic performance [26–28]. The presence of silanol groups (Si–OH) within the zeolite structure is pivotal in converting the inherently inactive silica matrix into a reactive functional platform [29]. The zeolite channels help prevent the aggregation of noble metal nanoparticles, thereby enhancing both the catalytic performance and longevity of the catalysts [30, 31]. Another significant challenge is the difficulty in ensuring that the active components enter the zeolite pores, leading to the formation of large nanoparticles on the external surface of the zeolite crystals. These nanoparticles can migrate and cause deactivation at high temperatures [32–35]. Additionally, metal cations tend to precipitate as bulk hydroxides in alkaline synthesis gels, resulting in the formation of large particles on the zeolite crystal surface. Therefore, it is crucial to develop effective protective strategies that can encapsulate the metal within the zeolite framework during the synthesis process.

Herein, Pt NPs encapsulated within nanosized S-1 zeolite (Pt@S-1) was successfully synthesized by the ligand-protected *in-situ* hydrothermal method. Notably, space-confined Pt NPs by the micropore structure of zeolite inhibit the sintering and aggregation of active ingredients, enabling the catalyst to display excellent catalytic activity and high-term stability under harsh conditions. The Pt species in the Pt@S-1 catalyst with well-stabilized inside the S-1 via Pt–O–Si bond displays exceptional catalytic performance and stability for soot oxidation, even after hydrothermal aging at 800 °C for 10 h. *In-situ* diffuse reflectance infrared Fourier transform spectroscopy (*in-situ* DRIFTS) spectra and density functional theory (DFT) calculations provide a valuable reaction mechanism. The *in-situ* encapsulation of Pt species significantly promotes the formation of NO_2 species, which plays a key role in the rate-determining step of soot oxidation. This work provides a promising approach for the rational design and synthesis of high-stability catalysts for the removal of soot particles in practical applications.

2 Experimental section

2.1 Synthesis of silicalite-1

The S-1 catalyst was synthesized using the hydrothermal method [36]. Typically, 8.32 g tetraethyl orthosilicate (TEOS) and 13 g tetrapropylammonium hydroxide solution (TPAOH, 25 wt.%) were mixed with 19.875 g deionized water at room temperature to form a clear solution. The obtained solution was magnetically stirred for 5 h at room temperature to achieve a homogeneous sol and ensure full hydrolysis of TEOS. The above mixtures were transferred to a 100 mL Teflon-lined autoclave and crystallized at 170 °C for 72 h. The solid precipitate was collected by centrifuging, washed several times with deionized water and ethanol, dried at 80 °C overnight, and then calcined at 550 °C in air for 6 h to remove the organic template.

2.2 Synthesis of Pt@S-1 catalyst

The preparation process of Pt@S-1 can be described as follows: Firstly, $H_2PtCl_6{\cdot}6H_2O$ and ethylenediamine (EDA) were mixed to form precursor solutions. The mixture was then subjected to ultrasonic treatment for 30 min, with the corresponding solution volumes for different Pt loads listed in Table S1 in the Electronic Supplementary Material (ESM). Next, the Pt@S-1 catalyst, with Pt nanoparticles confined within silicalite, was prepared using a one-pot hydrothermal method similar to the synthesis of S-1, with the addition of a specific amount of $H_2PtCl_6{\cdot}6H_2O$ and EDA. Specifically, 13 g TPAOH (25 wt.%) was mixed with 19.875 g of water. After stirring at room temperature for 30 min, an appropriate amount of precursor solution was added, and the mixture was stirred for an additional 30 min. Then, 8.32 g of TEOS was added into the solution, which was stirred at room temperature for 6 h. The mixture was hydrothermally treated at 170 °C for 72 h. The organic template was then removed after washing with distilled water and ethanol, followed by drying at 80 °C and calcining at 550 °C for 6 h in the air. Finally, the Pt@S-1 catalyst was obtained and denoted as Pt_n@S-1 (n = 0.06, 0.38, and 0.75), where n represents the actual Pt content. To highlight the advantages of encapsulation, an equivalent amount of Pt (0.38 wt.%) was added to the S-1 support by impregnation with a solution of $H_2PtCl_6{\cdot}6H_2O$. The impregnated sample was dried at 80 °C for 12 h and then calcined in air at 500 °C for 3 h. Finally, the 0.38 wt.% Pt/S-1 catalyst was obtained and denoted as $Pt_{0.38}$/S-1 catalyst.

2.3 Characterization

The crystal structure was characterized by X-ray diffraction (XRD) patterns on D8 Focus (Bruker AXS). The loading of Pt was measured by inductively coupled plasma optical emission spectrometry (ICP-OES). The morphology and particle size of the as-prepared catalysts were analyzed by scanning electron microscopy (SEM; SU8010), transmission electron microscopy (TEM; JEOL JEM 2100 LaB6), and probe-corrected scanning TEM (ACT-STEM, Hitachi HF5000) measurements. N_2 adsorption–desorption measurements were measured by BSD-PM (PM2-1561-A, Beishide instrument Technology Co., Ltd.). Ultraviolet–visible (UV–Vis) diffuse reflectance spectroscopy (DRS) measurements were recorded by UV-2600i (Shimadzu, Japan). The X-ray absorption fine structure (XAFS) spectra of Pt L_3-edge were measured at the beamline BL13SSW of Shanghai Synchrotron Radiation Facility (SSRF) in fluorescence mode. Hydrogen temperature-programmed reduction (H_2-TPR) measurements were carried out on a conventional flow apparatus with a thermal conductivity detector. X-ray photoelectron spectroscopy (XPS) measurements were conducted on a Thermo Scientific K-Alpha spectrometer. An online mass spectrometer apparatus detected the signal of NO temperature-programmed desorption (NO-TPD). Carbon monoxide temperature programmed surface reaction (CO-TPSR) was performed on a fixed-bed tubular quartz microreactor. CO chemisorption measurements were carried out *in-situ* DRIFTS with IRTracer-100. The NO temperature-programmed oxidation (NO-TPO) was carried out on a fixed-bed tubular quartz reactor. *In-situ* DRIFTS NO oxidation and soot oxidation experiments were recorded using a Shimadzu infrared spectrometer (IRTracer-100) over a range of 4000–800 cm^{-1}, and more experimental details were provided in the ESM.

2.4 Catalytic activity and stability evaluation

The catalytic activity of all catalysts for soot oxidation was evaluated by soot-temperature programmed oxidation (soot-TPO). The reactor was heated from 150 to 700 °C at a heating rate of 2 °C·min^{-1} in a stream of 0.1 vol.% NO and 10 vol.% O_2 balanced with N_2 at a total flow rate of 50 mL·min^{-1}. Printex-U from Degussa was used as the model soot in this study. The catalyst (100 mg) and soot (10 mg) were thoroughly mixed using a spatula for 10 min to simulate loose contact. The concentrations of CO and CO_2 in the outlet gas were monitored by online gas chromatography. Catalytic activity was evaluated and compared in terms of T_{10}, T_{50}, and T_{90} (T_{10}, T_{50}, and T_{90} correspond to the temperatures at which 10%, 50%, and 90% of soot conversion occurs, respectively.), which correspond to the temperatures at which 10%, 50%, and 90% of soot is converted, respectively. The selectivity of CO_2 formation (S_{CO_2}) was defined as the CO_2 outlet concentration (C_{CO_2}) divided by the sum of CO_2 and CO outlet concentration. $S_{CO_2}{}^m$ was denoted as the S_{CO_2} at which the C_{CO_2} value was the maximum. Catalyst stability was evaluated by recycling soot-TPO, long-term, and hydrothermal stability tests. To assess the hydrothermal stability of the $Pt_{0.38}$@S-1 and $Pt_{0.38}$/S-1 catalyst, 0.2 g of granular catalyst (40–60 mesh) was loaded inside a quartz tubular reactor and treated at 800 °C for 10 h in the presence of 10 vol.% H_2O/N_2. After naturally cooling to room temperature, the treated catalyst was ground into a powder and labeled $Pt_{0.38}$@S-1-HT (S-1-HT refers to the sample of S-1 zeolite after undergoing hydrothermal treatment) and $Pt_{0.38}$/S-1-HT. Subsequently, the catalyst (0.1 g) was mixed with soot (0.01 g) in loose contact for activity testing, and more experimental details were provided in the ESM.

2.5 DFT calculation

All spin-polarized DFT calculations were performed using the Vienna *ab initio* simulation package (VASP 5.4.4) [37]. The plane-wave basis set and the generalized-gradient approximation (GGA)-Perdew–Burke–Ernzerhof (PBE) functional were employed [38]. A $Si_{96}O_{192}$ model was used to represent silicalite-1 zeolite [39]. Four Pt atoms were employed to model Pt nanoparticles at the intersection between straight and sinusoidal ring channels [40]. The detailed calculation setting and models are described in the ESM.

3 Results and discussion

3.1 Design principle and structural characterizations

Pt nanoparticles encapsulated into S-1 zeolites was synthesized via a facile ligand-protected method (Fig. 1(a)), with the corresponding theoretical encapsulation model shown in Fig. 1(b). The XRD patterns of all catalysts exhibit the typical diffraction peaks of MFI zeolites at 2θ = 7.96°, 8.82°, 23.27°, 23.77°, and 23.97° (Fig. 1(c)), demonstrating that the MFI structure is preserved during the synthesis. The XRD diffraction peaks of the catalysts shift to lower angles, indicating that the metal ions have diffused into the zeolite framework (Fig. S1 in the ESM). Among all as-prepared catalysts, the diffraction peaks corresponding to the MFI structure shift to the highest angle for $Pt_{0.38}$@S-1 catalyst, which can be attributed to the abundant Pt species incorporated into the zeolite framework. The diffraction peaks corresponding to the crystal structure of Pt and PtO_2 are unobserved (Fig. 1(d)), indicating that the Pt component is highly dispersed and present at low loading in Pt_n@S-1 catalysts. ICP-OES results show that the actual Pt loading is lower than the theoretical content (Table S2 in the ESM), which can be attributed to Pt species loss during the co-hydrothermal synthesis process. Fourier transform infrared (FTIR) spectroscopy results suggest that zeolites with the MFI structure were successfully prepared (Fig. S2 in the ESM). Additionally, the interaction between the silanol groups and metal species was investigated by the FTIR spectra. The FTIR spectrum of the pure S-1 zeolite exhibits two major absorption peaks around 3725 and 3500 cm^{-1}, the one at 3725 cm^{-1} corresponds to external isolated silanol group (Fig. S3 in the ESM). The other band at 3500 cm^{-1} is associated with hydrogen-bond silanol group, i.e., silanol nests or defect sites [41]. With the Pt species introduced, the intensity of the hydroxyl groups decreases slightly, which can be assigned to Pt species that are predominantly trapped by silanol nets in the pores of S-1. The textural properties of the S-1 and Pt_n@S-1 catalysts were determined via N_2 physical adsorption–desorption measurements (Table S3 in the ESM). All catalysts exhibit similar type I isotherms with an H1-type hysteresis loop in the relative pressure range of 0–0.1, indicating the typical microporous structure of the MFI framework (Fig. 1(e)). A small H2-type hysteresis loop in the relative pressure range of 0.1–0.9 indicates the presence of mesopores, while an H3-type hysteresis loop in the relative pressure range of 0.9–1.0 suggests the formation of macropore structure. Notably, the specific surface area of $Pt_{0.38}$@S-1 catalyst decreased significantly (from 447 to 432 $m^2 \cdot g^{-1}$) compared to S-1, which can be attributed to the occupation of the S-1 channels by metal species. The micropore size of all catalysts is 0.536–0.578 nm (Fig. 1(f)), allowing reactant molecules to undergo reaction within the micropores, particularly the oxidation of NO to NO_2. Interestingly, the specific surface area of $Pt_{0.75}$@S-1 catalyst increases while mesoporosity decreases, which can be attributed to

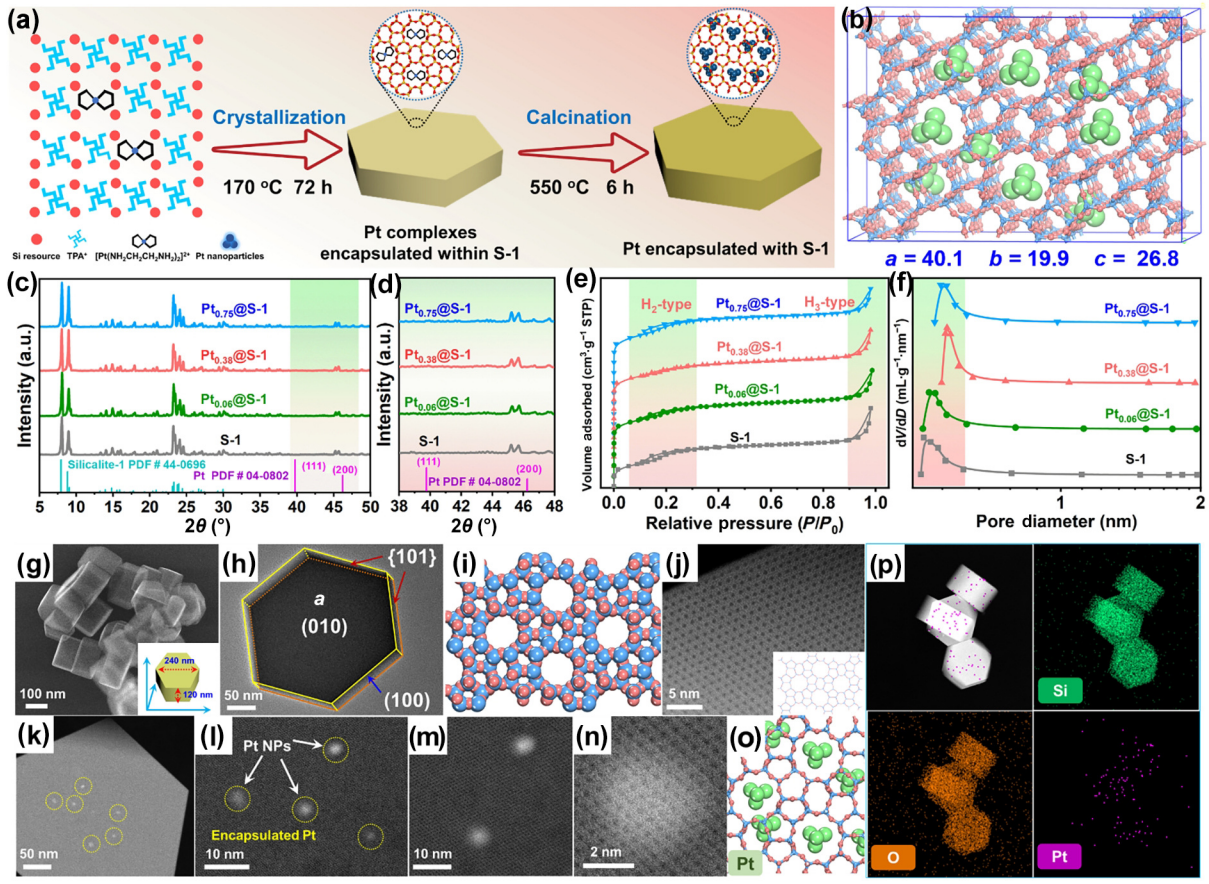

Figure 1 (a) Schematic of the preparation processes of Pt@S-1 catalyst. (b) Theoretical encapsulation model of Pt@S-1 catalyst. (c) XRD patterns and (d) the magnified patterns of Pt_n@S-1 catalysts. (e) N_2 adsorption–desorption isotherms and (f) pore size distribution curves of S-1 and Pt_n@S-1 catalysts. (g) STEM-SE and (h) TEM images of the S-1 catalyst. (i) The atom model of (010) crystal face of S-1. (j) STEM-ADF image of S-1 with scale bars of 5 nm. (k) STEM-ADF image for $Pt_{0.38}$@S-1 catalyst (Pt NPs are in the yellow circle). ((l) and (m)) STEM-ADF image of $Pt_{0.38}$@S-1 catalyst and the Pt NPs are dispersed in the yellow circle. (n) STEM-ADF image of magnified Pt NPs for $Pt_{0.38}$@S-1 catalyst. (o) The structural mode of $Pt_{0.38}$@S-1 catalyst. (p) STEM EDX elemental mapping images of $Pt_{0.38}$@S-1 catalyst.

the slight disruption of microstructure characteristics by the larger Pt nanoparticles.

The S-1 catalyst exhibits a uniform size and hexagonal prism morphology (Fig. 1(g)). The width and thickness of S-1 are approximately 240 and 120 nm, respectively, with two (010) and six (100) crystal faces (Fig. 1(h)). The S-1 catalyst has a single-crystal structure (Fig. S4 in the ESM), and the atomic-level mode of (010) crystal faces is shown in Fig. 1(i). The S-1 catalyst exhibits an abundant pore structure with a pore size of less than 1 nm (Fig. 1(j)), and branches are nucleated from the basal plane (010) faces (Fig. S5 in the ESM). The morphology and size of Pt@S-1 catalysts remain almost unchanged compared with S-1 (Fig. S6 in the ESM). The metal particles are not observed in the $Pt_{0.06}$@S-1 catalyst, indicating that Pt species are well dispersed throughout the entire S-1 zeolite (Fig. S7 in the ESM). In the STEM-SE (SE stands for secondary electrons) image of $Pt_{0.38}$@S-1 catalyst, no Pt metal particles are visible (Fig. S8 in the ESM), whereas the STEM-ADF (ADF stands for annular dark field) image of the same region reveals metal particles with a mean size of approximately 4 nm (Figs. 1(k)–1(n)). This indicates that the Pt NPs are dispersed within the inner part of the S-1 crystal but are not visible on the outer surface. The Pt NPs are located within the intersectional channels between the straight and sinusoidal 10-ring channels of the MFI framework. The visually observed size of the Pt species appears larger than the MFI channels (Fig. 1(n)), which can be attributed to the encapsulated metal species between the straight and sinusoidal channels of the MFI structure. Therefore, the Pt NPs are anchored inside the zeolite framework (Figs. 1(n) and 1(o)). The Pt size of the $Pt_{0.38}$/S-1 catalyst is about 18 nm (Fig. S9 in the ESM), and the energy-dispersive X-ray spectrometry (EDX) mapping results further confirm the severe aggregation of Pt species on the surface of S-1 (Fig. S10 in the ESM). The STEM EDX mapping images of $Pt_{0.38}$@S-1 catalyst show the uniform dispersion of Pt NPs (Fig. 1(p)). As the Pt loading increases, anomalous large Pt NPs (12 nm) are found on the surface of zeolite, as indicated by white arrows (Fig. S11 in the ESM). Additionally, with increasing Pt loading, a broader absorption peak gradually appears around 250 nm in UV–Vis spectra, which can be attributed to subnanometric Pt clusters inside zeolitic pores (Fig. S12 in the ESM) [42]. These observations further confirm that the Pt NPs are confined within the S-1 zeolite.

3.2 Chemical structure and oxidation property

To determine the chemical state of the Pt NPs, Raman, CO-DRIFT, XPS, X-ray absorption near-edge structure (XANES), and the extended XAFS (EXAFS) spectra were employed to investigate the characterizations of the Pt@S-1 and Pt/S-1 catalysts [43]. Obvious characteristic bands of MFI zeolite structure at 295 and 475 cm^{-1} are observed in all prepared catalysts (Fig. 2(a)), which can be assigned to bending vibrations of the six-ring and four-membered rings in

the zeolite, respectively. The bands at 379 and 436 cm^{-1} are attributed to the stretching vibration of the Si–O–Si bonds and the asymmetric stretching vibration of the Pt–O–Si bonds, respectively [44]. The two weak bands at 436 and 544 cm^{-1} are assigned to the PtO (E_g) and PtO_2, respectively [45]. In contrast, the $Pt_{0.75}$@S-1 catalyst exhibits two strong bands corresponding to PtO_x, indicating the formation of larger Pt NPs in the $Pt_{0.75}$@S-1 catalyst. *In-situ* DRIFTS measurement with CO adsorption was used to investigate the electronic state of Pt active sites in the catalysts (Fig. 2(b)). For the $Pt_{0.38}$@S-1 catalyst, four peaks located at 2100, 2087, 2046, and 1882 cm^{-1} can be reasonably attributed to CO adsorption on Pt_xO_y ensembles [46], linearly adsorbed CO on $Pt^{\delta+}$ single-atoms [47], CO adsorbed on Pt^0 nanoparticles with different sizes [48], and bridge coordinated CO molecules on Pt sites [49], respectively. Linearly adsorbed CO on $Pt^{\delta+}$ (2087 cm^{-1}) is undetected on the $Pt_{0.38}$/S-1 catalyst (Fig. S13 in the ESM). Thus, Pt species coexist as metallic Pt and oxidized Pt species in the $Pt_{0.38}$@S-1 catalyst, while the $Pt_{0.38}$/S-1 catalyst contains only Pt NPs. Additionally, the XPS spectra of the Pt 4f region display two components for Pt@S-1 catalyst, corresponding to Pt^0 and Pt^{n+} species (Fig. S14 in the ESM).

XAFS measurements were performed to reveal the atomic configurations of Pt species on the $Pt_{0.38}$@S-1 catalyst. The Pt L_3-edge XANES spectra of the $Pt_{0.38}$@S-1 catalyst display that the white line peak intensity is much weaker than that of PtO_2 while is slightly higher than that of Pt foil (Fig. 2(c)), indicating that the valence state of Pt in the $Pt_{0.38}$@S-1 catalyst contained more positive charges than that of Pt foil but fewer positive charges than that of PtO_2 [50–52]. The EXAFS spectra of $Pt_{0.38}$@S-1 catalyst show a primary peak at 2.64 Å, corresponding to the Pt–Pt bond (Fig. 2(d)). Additionally, the coordination number of first-shell Pt–Pt bonding for the $Pt_{0.38}$@S-1 catalyst is about 9.3, indicating that the Pt NPs are of small size (Fig. S15 and Table S4 in the ESM). The strong wavelet transform (WT) signal appears at 6–14 $Å^{-1}$ in *k* space (Fig. S16 in the ESM), ascribing to the Pt–Pt bond. Additionally, the WT of the k^3-weighted EXAFS spectra provide structural information in both *R* space and *k* space. The intensity and contour plot of $Pt_{0.38}$@S-1 differs from that of Pt-foil, further confirming the predominance of Pt–Pt bonds with only a small amount of Pt–O bonds on the surface of $Pt_{0.38}$@S-1 catalyst (Fig. 2(e)). This phenomenon can be attributed to the strong interaction between embedded Pt particles and skeleton oxygen.

The H_2-TPR experiments were conducted to characterize the

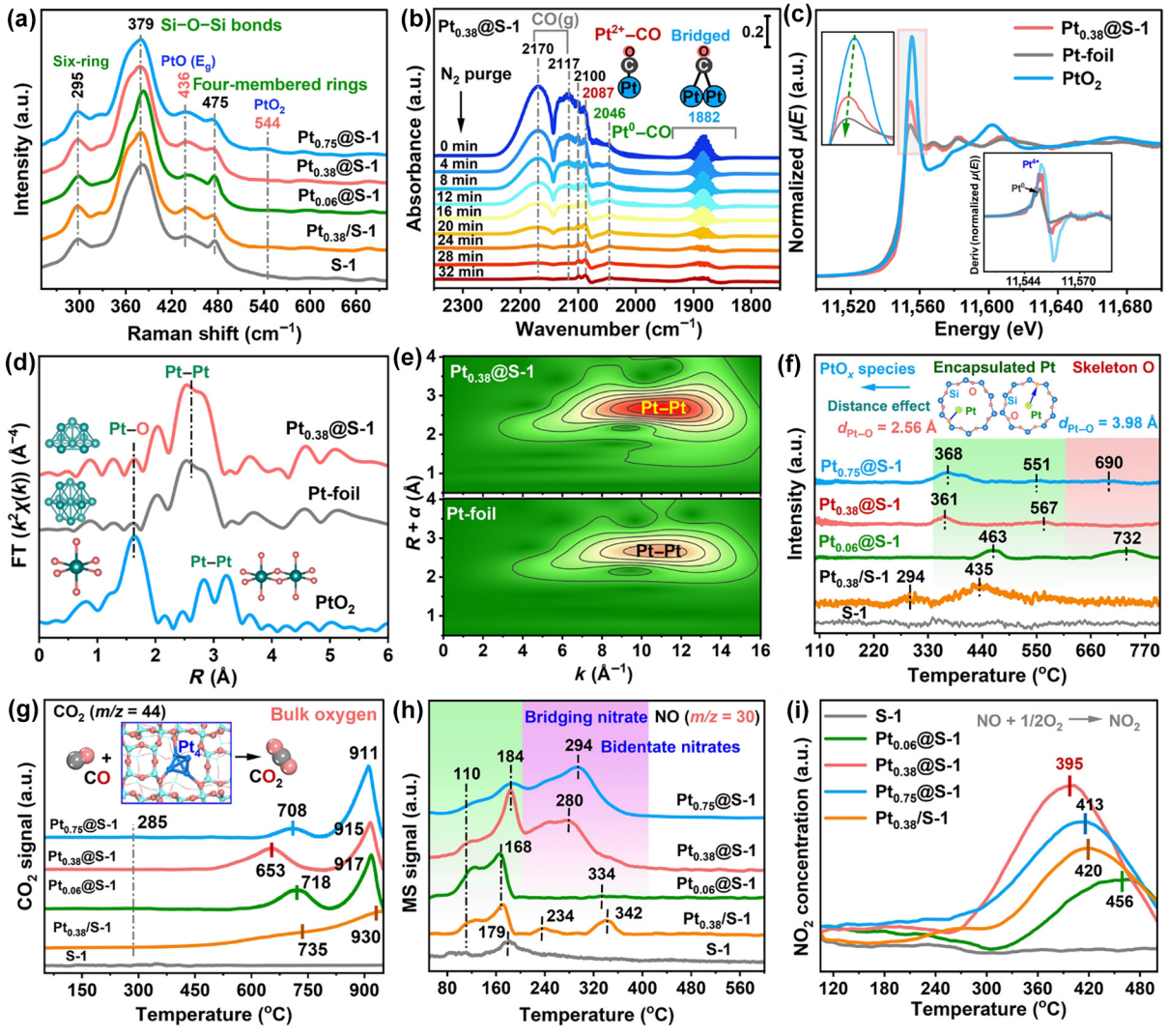

Figure 2 (a) Raman spectra with an excitation wavelength of 325 nm. (b) *In-situ* DRIFTS of CO adsorption at 30 °C. (c) The Pt L_3-edge XANES spectra. (d) Pt L_3-edge Fourier transforms curves of EXAFS oscillations of $k^2\chi(k)$. (e) Pt L_3-edge WT-EXAFS spectra of $Pt_{0.38}$@S-1. (f) H_2-TPR and (g) CO-TPSR profiles of Pt_n@S-1 and $Pt_{0.38}$/S-1 catalysts. (h) NO-TPD and (i) NO-TPO profiles of Pt_n@S-1 and $Pt_{0.38}$/S-1 catalysts.

redox properties of the catalysts. As shown in Fig. 2(f), the TPR profile of the S-1 catalyst shows no reduction peaks. The $Pt_{0.38}$/S-1 catalyst exhibits two reduction peaks at 294 and 435 °C, which can be assigned to the reduction of PtO_x with weak and strong interactions between the PtO_x species and the S-1 support, respectively [53]. The Pt@S-1 catalysts show no reduction peaks at the temperature range of 100–300 °C, which can be attributed to the encapsulated Pt nanoparticles located within the pore channels of the S-1. The reduction peak of the $Pt_{0.38}$@S-1 catalyst observed between 300–600 °C, is assigned to the reduction of oxygen in the zeolite skeleton near encapsulated Pt NPs. The $Pt_{0.38}$@S-1 catalyst displays the lowest reduction peak at 361 °C, suggesting that the encapsulated Pt NPs are close to the skeleton oxygen and that there is an interaction between Pt and the S-1 framework. It indicates that the introduction of Pt species significantly enhances the oxidation capacity and weakens the intensity of the Si–O bond. Additionally, CO can be used as a probe molecule to study active oxygen species on the catalyst surface (Fig. 2(g)). The skeleton oxygen can be activated to form active oxygen species by the interaction between Pt and S-1. The $Pt_{0.38}$@S-1 catalyst shows the lowest temperature peaks at 653 °C, further suggesting that Pt NPs are close to the oxygen atom in the $Pt_{0.38}$@S-1 catalyst.

To evaluate the NO_x storage capacity of all the as-prepared catalysts, the NO_x desorption behaviors were studied using the TPD technique (Fig. 2(h)). The weak shoulder peak at 110 °C is attributed to the desorption of weakly adsorbed NO and the decomposition of surface nitrites (< 200 °C) [54]. The desorption peaks in the range of 200–400 °C can be assigned to bridging nitrate and bidentate nitrates species. $Pt_{0.38}$@S-1 catalyst exhibits a large decomposition peak area, indicating its excellent NO_x storage capacity. NO-TPO measurements were conducted to investigate the activation property of the catalyst for NO molecules (Fig. 2(i)). The S-1 catalyst exhibits poor oxidation ability for NO oxidation. However, after the introduction of Pt species, the NO_2 peak shifts to a lower temperature. The $Pt_{0.38}$@S-1 catalyst shows the highest concentration of NO_2 and corresponds to the lowest peak temperature at 395 °C. The highly dispersed Pt species in the $Pt_{0.38}$@S-1 catalyst provide a greater number of active sites, promoting the formation of large amounts of active oxygen species, which is consistent with the results of O 1s XPS spectra (Fig. S17 and Table S5 in the ESM). The larger fraction of active oxygen species may readily participate in the NO oxidation to form NO_2 oxidant. Thus, the $Pt_{0.38}$@S-1 catalyst exhibits superior catalytic activity for soot oxidation, which can be assigned to the excellent oxidation performance for NO molecules.

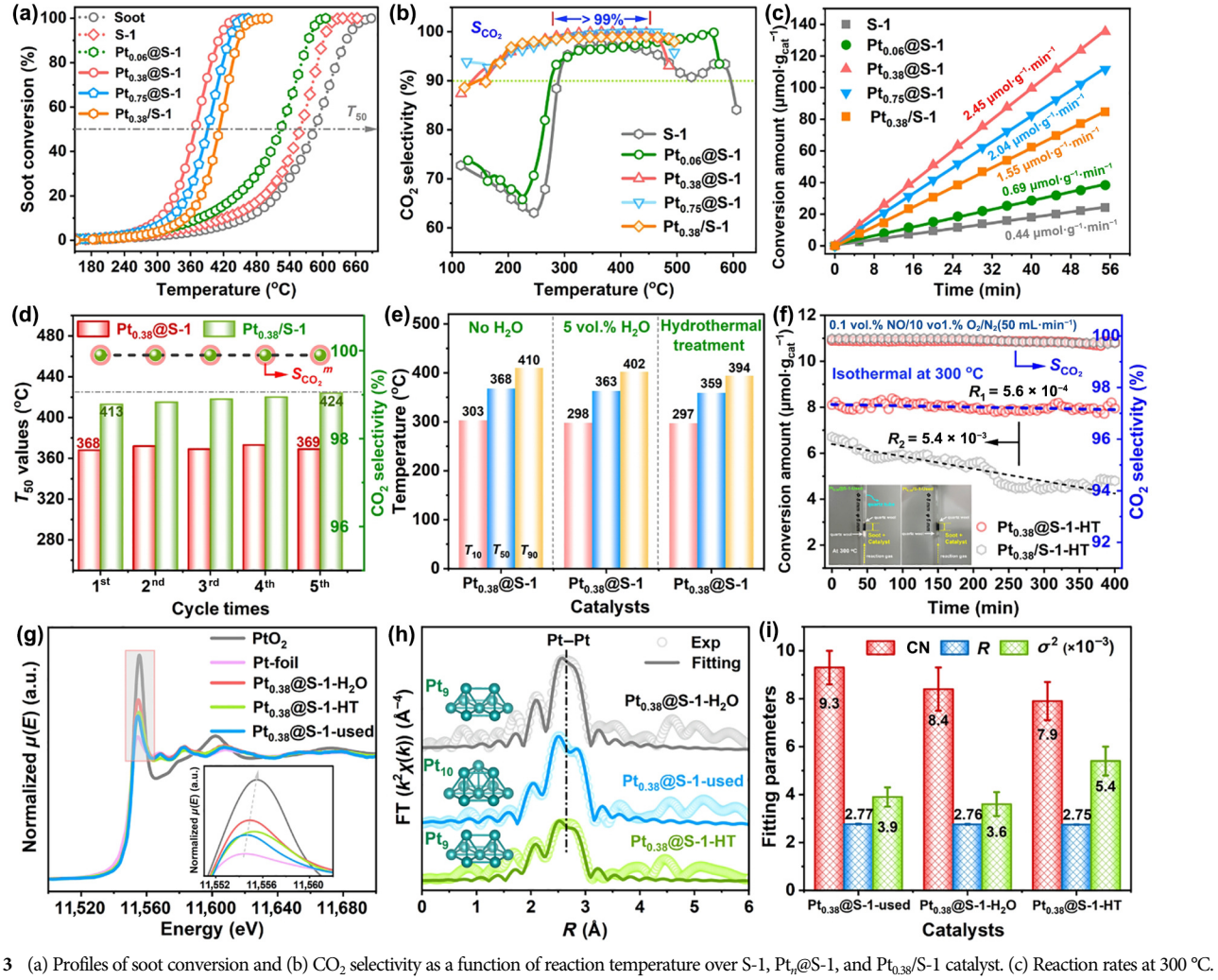

Figure 3 (a) Profiles of soot conversion and (b) CO_2 selectivity as a function of reaction temperature over S-1, Pt_n@S-1, and $Pt_{0.38}$/S-1 catalyst. (c) Reaction rates at 300 °C. (d) Recycle stability tests over $Pt_{0.38}$@S-1 and $Pt_{0.38}$/S-1 catalysts. (e) H_2O-tolerance performance of $Pt_{0.38}$@S-1 catalyst for soot oxidation. (f) Long-term catalytic stability evaluation at 300 °C for $Pt_{0.38}$@S-1-HT and $Pt_{0.38}$/S-1-HT catalysts. ((g) and (h)) XANES spectra (g) and EXAFS spectra (h) of the Pt L_3-edge of $Pt_{0.38}$@S-1-used, $Pt_{0.38}$@S-1-H_2O, and $Pt_{0.38}$@S-1-HT catalysts. (i) Fitting parameters of Pt L_3-edge EXAFS.

3.3 Catalytic activity and stability for soot oxidation

The catalytic activities of all as-prepared catalysts for soot oxidation were investigated by the soot-TPO reaction (Fig. 3(a) and Table S6 in the ESM). The S-1 support exhibits low catalytic activity for soot oxidation, with T_{50} and $S_{CO_2}{}^{m}$ values are 558 °C and 59.7%, respectively. However, after the introduction of the Pt species, the catalytic performance improves significantly, enhancing the efficiency of soot oxidation. Among all as-prepared catalysts, the $Pt_{0.38}$@S-1 catalyst exhibits the highest activity for soot oxidation; i.e., the T_{10}, T_{50}, and T_{90} values are 303, 368, and 410 °C, respectively. However, the catalytic performance decreases for the $Pt_{0.75}$@S-1 catalyst, which can be attributed to the reduced dispersion of Pt species at high loading, leading to a decrease in the number of active sites on the catalyst. To highlight the advantages of encapsulation, $Pt_{0.38}$/S-1 catalyst was prepared as a comparison. The $Pt_{0.38}$@S-1 catalyst demonstrates higher catalytic activity compared to the $Pt_{0.38}$/S-1 catalyst (T_{50} = 412 °C), indicating that the encapsulated Pt species provide more active sites for reaction molecules. The CO_2 selectivity of the $Pt_{0.38}$@S-1 catalyst reaches nearly 100%, and this high selectivity is maintained over a wide temperature range from 300 to 500 °C (Fig. 3(b)). The relative conversion rate (CR) was calculated from the isothermal oxidation reactions of the catalysts at 300 °C (Fig. 3(c)). Upon introducing Pt species, the CR values increased significantly. The $Pt_{0.38}$@S-1 catalyst shows the highest CR value (2.45 $\mu mol \cdot g^{-1} \cdot min^{-1}$), which is 1.58 times higher than that of the $Pt_{0.38}$/S-1 catalyst. This indicates that the highly dispersed Pt species provides additional sites for adsorption–activation reaction reactants.

To further evaluate the catalytic stability, recycled soot-TPO tests were performed. Over five cycles of soot-TPO tests (Fig. 3(d)), the temperature difference of T_{50} for the $Pt_{0.38}$/S-1 catalyst increases significantly (ΔT_{50} = 11 °C) compared to the $Pt_{0.38}$@S-1 catalyst (ΔT_{50} = 1 °C). After five cycles of soot-TPO experiments, the XRD patterns of $Pt_{0.38}$@S-1 remain unchanged, and the morphology still retains its hexagonal prism structure (Fig. S18 in the ESM). The XAFS measurement of the used $Pt_{0.38}$@S-1 catalyst ($Pt_{0.38}$@S-1-used) was performed to obtain coordination information (Figs. 3(g)–3(i) and Fig. S19 in the ESM). The Pt L_3-edge XANES spectra of $Pt_{0.38}$@S-1-used are very similar to that of the fresh $Pt_{0.38}$@S-1 catalyst. The average coordination number of Pt–Pt bonds is 9.3 ± 0.7 based on EXAFS results, which is similar to that of the fresh sample, indicating that the $Pt_{0.38}$@S-1 has excellent recycle stability during soot oxidation. The hydroxyl groups in zeolites serve as anchoring sites for metal species, thereby preventing metal agglomeration and subsequent catalyst deactivation. In partial working conditions, other components of vehicle emissions (NO and H_2O) can influence the catalytic activity. To investigate the effect of NO on the performance of the catalyst, the activity tests of $Pt_{0.38}$@S-1 catalyst were conducted under conditions of gradient concentration of NO (Fig. S20 in the ESM). The T_{50} value of $Pt_{0.38}$@S-1 is 554 °C in the absence of NO. After the introduction of the NO into the reaction system, the catalytic performance improves significantly, with the T_{50} value decreasing from 554 to 368 °C as the NO concentration increases from 0 vol.% to 0.1 vol.%. However, further increases in the NO concentration (0.2 vol.%) do not result in additional enhancement of catalytic activity, suggesting that there is an optimal NO concentration that can significantly promote soot oxidation.

Water vapor (5 vol.%) was introduced into the reaction gas during soot oxidation (Fig. 3(e) and Fig. S21 in the ESM). The T_{50} value of $Pt_{0.38}$@S-1 catalyst hardly changed after the introduction of water vapor, indicating its high resistance to H_2O. This high stability was further confirmed by hydrothermal aging tests, where the T_{50} value of $Pt_{0.38}$@S-1-HT catalyst decreases by only 9 °C after hydrothermal treatment. Additionally, a long-term catalytic stability evaluation was conducted for the $Pt_{0.38}$@S-1-HT and $Pt_{0.38}$/S-1-HT catalysts (Fig. 3(f)). The amount of soot conversion over $Pt_{0.38}$/S-1-HT catalyst rapidly decreased within 400 min, while the conversion amount of the $Pt_{0.38}$@S-1-HT catalyst remained nearly unchanged. The deactivation rate of $Pt_{0.38}$/S-1-HT is 10-fold that of the $Pt_{0.38}$@S-1-HT catalyst, implying that the $Pt_{0.38}$@S-1 catalyst has excellent H_2O-resistance compared with the $Pt_{0.38}$/S-1 catalyst. The presence of a black mixture is different from the catalyst color in the quartz tube after the long-term reaction because soot particles were not completely consumed (Fig. 3(f)). The XAFS measurements were performed to determine the electronic state and coordination environment of the Pt NPs in the $Pt_{0.38}$@S-1 catalyst after the exposure of water vapor ($Pt_{0.38}$@S-1-H_2O) and hydrothermal treatment (Figs. 3(g)–3(i)). The Pt L_3-edge XANES spectra of both the $Pt_{0.38}$@S-1-H_2O and $Pt_{0.38}$@S-1-HT catalyst show an increased oxidation state for two Pt atoms compared to the fresh $Pt_{0.38}$@S-1 catalyst (Fig. 3(g)). In the Pt L_3-edge EXAFS results, the average coordination number of Pt–Pt bonds in the $Pt_{0.38}$@S-1-H_2O and $Pt_{0.38}$@S-1-HT catalysts are found to be 8.4 ± 0.9 and 7.9 ± 0.8, respectively (Figs. 3(h) and 3(i) and Table S4 in the ESM). A discernible diminution in the Pt–Pt coordination number was observed following steam and hydrothermal treatments when compared to the fresh $Pt_{0.38}$@S-1 catalyst. Compared with the fresh $Pt_{0.38}$@S-1 catalyst, the intensity of hydroxyl nests in $Pt_{0.38}$@S-1-HT and used $Pt_{0.38}$@S-1-H_2O catalysts decreased to some extent (Fig. S22 in the ESM). This phenomenon can be attributed to that prolific hydroxyl species generated during steam exposure and hydrothermal treatment protocols effectively mediate the dispersion and stabilization of Pt species within the catalyst matrix [55]. Combined with the above contrast experiment results, it indicates that the *in-situ* encapsulated $Pt_{0.38}$@S-1 catalyst exhibits excellent catalytic activity, durability, and H_2O tolerance compared to the $Pt_{0.38}$/S-1 catalyst prepared by the traditional impregnated method.

3.4 *In-situ* DRIFT spectra and DFT calculations

Forming NO_2 species is crucial because NO_2 has stronger oxidation properties and follows the NO_x-assisted mechanism during soot oxidation. Therefore, a catalyst with excellent activation performance for NO molecules is beneficial for promoting soot oxidation at lower temperatures. To study the NO adsorption behavior on the surface of S-1 and $Pt_{0.38}$@S-1 catalyst, *in-situ* DRIFTS measurements were performed (Fig. 4(a) and Fig. S23 and Table S7 in the ESM). The NO adsorption species formed on the $Pt_{0.38}$@S-1 catalyst is similar to those observed on the S-1 catalyst. The adsorption peaks observed at 1764, 1656, 1425, 1365, and 920 cm^{-1} are attributed to trans-$N_2O_2^{2-}$, bridge nitrites, monodentate nitrites, monodentate nitrates peak, and NO_2/N_2O_4 species, respectively [56–60]. Notably, the monodentate nitrites (1425 cm^{-1}) disappeared, while the new band was detected at 1405 cm^{-1}, which can be assigned to trans-$N_2O_2^{2-}$ species [61]. No peaks related to free NO species were detected at lower temperatures, likely due to the tendency of gas-phase NO molecules to readily bind to the Lewis acid sites on the catalyst, owing to their single electron bond structure [62]. The NO adsorption reached saturation within 30 min, and the $Pt_{0.38}$@S-1 catalyst showed stronger adsorption

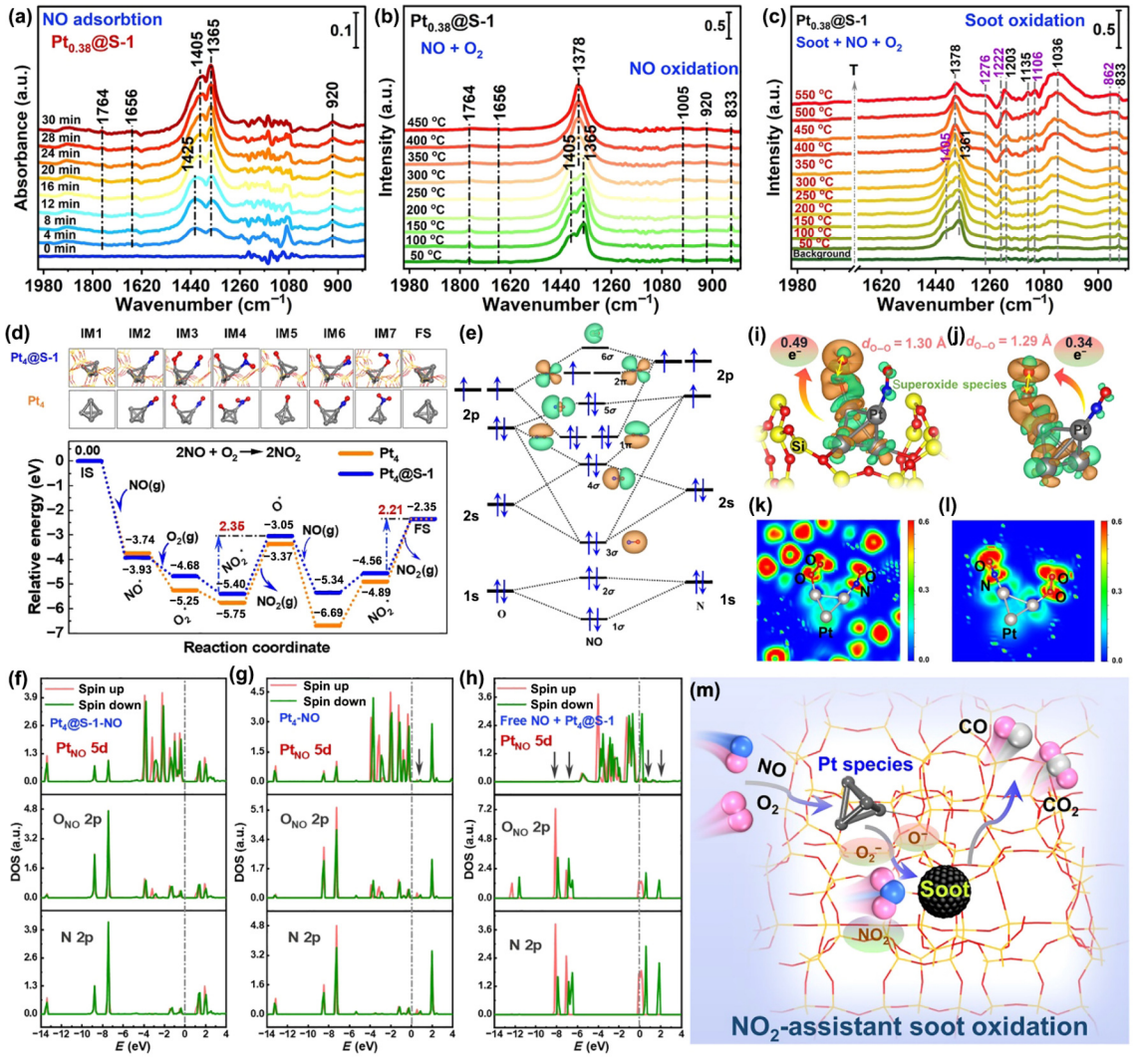

Figure 4 ((a)–(c)) *In-situ* DRIFT spectra of NO adsorption (a), NO oxidation (b), and soot oxidation (c) over $Pt_{0.38}$@S-1 catalyst. (d) Reaction pathway for NO oxidation on Pt_4@S-1 catalyst. (e) The major interactions and energy levels of the molecular orbits for the NO molecule. ((f)–(h)) PDOS plots for NO adsorbed on the Pt sites in Pt_4@S-1 (f), isolate Pt_4 (g), and PDOS plots for a free NO molecule and the Pt_4@S-1 (h). ((i) and (j)) Differential charge density map increase (brown color) and decrease (green color) of electron distribution for Pt_4@S-1 (i) and Pt_4 (j). ((k) and (l)) ELF analyses for O_2 adsorbed on Pt_4@S-1 (k) and Pt_4 (l). (m) The route of soot oxidation is proposed based on the experimental and theoretical simulation results.

compared to the S-1 catalyst (Fig. S24 in the ESM). This suggests that the NO adsorption capacity is significantly enhanced with the introduction of Pt species.

In-situ DRIFTS measurements were conducted at various temperatures to further investigate the surface intermediates during NO oxidation (Fig. 4(b) and Fig. S25 in the ESM). At a relatively low temperature of 50 °C, a series of NO_x-containing species were detected on the surface of the $Pt_{0.38}$@S-1 catalyst. These species include trans-$N_2O_2^{2-}$ (1764 and 1405 cm^{-1}), bridge nitrites (1656 cm^{-1}), monodentate nitrates (1365 cm^{-1}), NO_2/N_2O_4 species (920 cm^{-1}), and bending vibration of nitrates (833 cm^{-1}). Notably, as the reaction temperature increases, the bands corresponding to trans-$N_2O_2^{2-}$, bridge nitrites, monodentate nitrates, and bending vibration of nitrates gradually weaken and eventually disappear. Simultaneously, a new characteristic peak appears at 1380 cm^{-1} above 250 °C, which can be assigned to ionic nitrates species. The intensity of ionic nitrates gradually weakens from 250 to 450 °C, indicating that the ionic nitrates species gradually decompose. Thus, NO is readily oxidized to NO_2 on the $Pt_{0.38}$@S-1 catalyst. The nitrate/nitrite species serve as key intermediates in the NO oxidation process, and the NO_2 released from these species subsequently promotes soot oxidation. To study the effect of NO and O_2 on the competitive adsorption of active sites, NO and O_2 were simultaneously injected into the reaction system on both S-1 and $Pt_{0.38}$@S-1 catalysts. The intensity of NO_x-species significantly decreased for $Pt_{0.38}$@S-1 catalyst after the simultaneous injection of NO and O_2, indicating the competitive adsorption between NO and O_2 (Fig. S26 in the ESM). This result is consistent with the catalytic performance at varying NO concentrations, suggesting that the Pt species serve as active sites for both NO and O_2 molecules. Therefore, the introduction of Pt species enhances the decomposition of ionic nitrates, promoting the formation of NO_2 species.

To further investigate the influence of NO_x species on soot oxidation over the S-1 and $Pt_{0.38}$@S-1 catalysts, *in-situ* DRIFTS measurements were conducted for both catalysts with soot in the presence of NO and O_2. *In-situ* DRIFTS spectra of adsorbed species on the soot-free catalyst in the reaction atmosphere were also

recorded (Fig. S27 and Table S7 in the ESM). A series of surface-oxygen complexes (SOCs) were detected on the soot surface. The containing N-species and C-species on the surface of the catalyst-soot were recorded in the reaction atmosphere (Fig. 4(c)). The bands in the spectra of pure soot and the catalyst-soot mixtures exhibit significantly lower intensity, which can be attributed to the strong light-absorbing properties of soot. A series of bands can be detected on the $Pt_{0.38}$@S-1 catalyst, primarily corresponding to the symmetric stretch vibrations of chelating bidentate carbonates (1585 cm^{-1}), COO^- vibration of acetate species (1405 cm^{-1}), ionic nitrates (1378 cm^{-1}), monodentate nitrates (1365 cm^{-1}), bidentate nitrates (1036 cm^{-1}), vibration of C=O in aromatic ester groups (1726 cm^{-1}), anti-symmetric stretch vibrations of chelating bidentate carbonates (1222 cm^{-1}), nitrito bidentate groups (1203 cm^{-1}), free nitrate (1135 cm^{-1}), C–N stretching vibration (1106 cm^{-1}), and carbonate species (862 cm^{-1}). With the rising reaction temperature, the monodentate nitrates species and COO^- vibration of acetate species gradually weaken and eventually disappear (below 250 °C). The ionic nitrates species begin to decompose at 300 °C, and the intensity of bridge nitrates and free nitrates gradually increases. Meanwhile, the intensities of symmetric stretch vibration of chelating bidentate carbonates, nitrito bidentate species, anti-symmetric stretch vibrations of chelating bidentate carbonates, C–N stretching vibration, and carbonate species gradually increase with rising the temperature. The S-1 catalyst shows a similar process to the $Pt_{0.38}$@S-1 catalyst for soot oxidation (Fig. S28 in the ESM). However, the $Pt_{0.38}$@S-1 catalyst shows C–N stretching vibration species at a lower temperature (100 °C) compared to the S-1 catalyst, suggesting that the formation of NO_2 by NO oxidation on the $Pt_{0.38}$@S-1 catalyst can be adsorbed to the surface of soot, leading to the formation of CO and CO_2 products.

The electron and energy evolution progress of the surface-active intermediate over Pt_4@S-1 and Pt_4 were further investigated using DFT calculations (Fig. S29 in the ESM). The reaction pathway and the corresponding relative energy changes during NO oxidation can be divided into eight stages as follows (Fig. 4(d)). Firstly, a gaseous NO molecule adsorbs at the vertex position of the Pt NPs, forming an O–N–Pt bond adsorbs at the intersection between the straight and sinusoidal ring channels (NO*; IM1 (IM1 stands for intermediate 1)). The adsorption energies of NO (E_{ads}(NO)) are −3.93 and −3.74 eV for Pt_4@S-1 and Pt_4, respectively, indicating that the Pt site exhibits enhanced adsorption of the NO molecule after the formation of the encapsulation structure. The N–O bond length and the O–N–Pt bond angle for NO adsorption on Pt_4@S-1 catalyst are 1.19 Å and 170.2°, respectively. In contrast, NO adsorption on Pt_4 exhibits a similar N–O bond length (1.19 Å) but a large O–N–Pt bond angle of 177.6°. This adsorption geometry on Pt_4 is close to a linear arrangement of NO at the Pt sites, which can be attributed to the steric hindrance effects influencing the structure of NO adsorption. The Pt atom serves as the central atom in the catalytic reaction, and the unpaired electrons in the 5d orbital readily hybridize with the unpaired electrons in the N 2p orbital of the NO molecule (Fig. 4(e)). Upon NO adsorption, the projected density of states (PDOS) plot of the Pt atomic orbital shifts to lower energies. In contrast, the PDOS plots of the N and O_{NO} (O_{NO} comes from the NO molecule) atomic orbital show significant charges compared to those of the free NO molecule (Figs. 4(f)–4(h)), as evidenced by a shift to higher energies and the emergence of new peaks in the range of new peaks in the range from 0 to −4 eV. Additionally, after NO adsorption, the spin of the electron states of N and O_{NO} becomes symmetric, indicating the involvement of extra electrons and the formation of strong covalent bonds between N and O atoms. The nature of the interaction between the adsorbed NO and the Pt sites can be further characterized by electron localization function (ELF) charge density difference (CDD). The ELF plots for Pt_4@S-1 reveal a strong electronic interaction between the NO and Pt_4@S-1 (Figs. S30 and S31 in the ESM).

Secondly, an O_2 molecule adsorbs on another Pt site through an O–O–Pt bond, forming a surface-adsorbed O_2* (O_2*; IM2). The total net charge transfer from the Pt_4@S-1 surface to the O_2 molecule is 0.54e^-, while for isolated Pt_4 NPs, it is 0.34e^- (Figs. 4(i) and 4(j) and Figs. S32 and S33 in the ESM). This suggests that encapsulated Pt_4 NPs are more effective in activating the O=O bond, facilitating the formation of activated oxygen species. The ELF plot for Pt_4@S-1 shows a greener color between the O and Pt atoms compared to Pt_4 (Figs. 4(k) and 4(l)), indicating the presence of a strong ionic bond. The shorter bond length and larger value of −COHP suggest that the O–O bond is more difficult to break on Pt_4 (ICOHP = −6.89 eV) than on Pt_4@S-1 (ICOHP = −6.82 eV). This implies that the O_2 molecule is less easily activated to form reactive oxygen species on isolated Pt_4 compared to Pt_4@S-1 catalyst (Fig. S34 and Table S8 in the ESM). Thirdly, the adsorbed NO combines with O* to form the surface intermediate NO_2 species (NO_2*; IM3). Fourth, the NO_2* species desorbs from the surface of the Pt_4 NPs (IM4). Fifth, an additional NO molecule adsorbs on O* to form ONO* (IM5). Finally, the NO_2* species desorbs from the surface of Pt_4 NPs, completing the reaction cycle (final state (FS)). The NO_2 desorption energy (E_{des}(NO_2)) for Pt_4@S-1 (1.87 eV) is lower than that for isolate Pt_4 NPs (2.05 eV), indicating that the NO_2 molecule is more readily desorbed from the Pt_4 NPs. In summary, the encapsulated Pt species enhance NO adsorption, and the formation of active oxygen species promotes the oxidation of NO to the NO_2 intermediate. This intermediate is easily desorbed from the surface of the encapsulated Pt_4 NPs, aided by steric hindrance, resulting in the formation of highly mobile and strong oxidizing NO_2 (g).

Based on the above discussion and experimental results, the encapsulated Pt@S-1 catalyst exhibits excellent catalytic activity and superior stability for soot oxidation. To further investigate the origin of the catalytic activity of the Pt sites in Pt@S-1, the PDOS plots for the two models are shown in Fig. S35 in the ESM. The *d*-band center of Pt atoms in Pt@S-1 is closer to the Fermi level compared to isolate Pt_4. This higher *d*-band center in Pt@S-1 results in the presence of empty anti-bonding states, which enhances the bond strength with adsorbates. The catalytic pathway for soot oxidation over the Pt_4@S-1 catalyst is outlined below, with a schematic diagram shown in Fig. 4(m). The encapsulated Pt NPs increase the density of active sites and effectively prevent catalyst deactivation. Ultimately, NO_2 can migrate to the soot surface, where it oxidizes the soot to form CO and CO_2. The by-product CO can then be further oxidized by active oxygen species to form CO_2. The oxidation of NO to NO_2 is a key step in soot oxidation, and the catalytic performance of soot oxidation is closely related to the activity of the catalyst to NO molecule.

4 Conclusion

In this work, Pt NPs (4 nm) were successfully confined within the zeolite S-1 framework by *in-situ* assembly crystallization. The high dispersion of Pt species achieved by *in-situ* synthesis increases the

density of active sites for reactant molecules. Additionally, the spatial confinement of Pt nanoparticles and abundant hydroxyl sites within the zeolite framework effectively prevents the aggregation of Pt species to improve catalyst stability. Among all the as-prepared catalysts, the $Pt_{0.38}$@S-1 catalyst shows superior catalytic performance (T_{50} = 368 °C; $S_{CO_2}^{m}$ = 99.9%) and high stability (cycle stability and long-term stability) during soot oxidation under loose contact conditions. Conspicuously, the reaction rate of the confined $Pt_{0.38}$@S-1 catalyst is 1.58-fold than that of the conventional $Pt_{0.38}$/S-1 catalyst. Through characterizations and DFT calculations, the reaction mechanism is revealed: *In-situ* encapsulated Pt species ensure a high density of active sites, which promote the adsorption and activation of O_2 to form active oxygen species. These active oxygen species can boost NO oxidation to NO_2. Meanwhile, the encapsulated Pt in the Pt@S-1 catalyst exhibits a higher *d*-band center than isolated Pt species, which enhances its bonding strength for the co-adsorption of NO and O_2 molecules. The formation of NO_2 is more easily desorbed from the surface of the encapsulated Pt NPs, which is a crucial step in the NO_2-assisted catalytic mechanism for soot oxidation. Finally, the formation of gaseous NO_2 can migrate to the soot surface along with the reaction gas flow, oxidizing the soot to form CO_2. This work provides a promising approach for the rational design and synthesis of high-stability catalysts for soot oxidation in practical applications.

Electronic Supplementary Material: Supplementary material (detail of the experimental section, characterization methods, catalytic activity and stability test, XRD patterns, FTIR spectra, TEM images, STEM-SE images, EDX mapping images, UV–Vis, CO adsorption DRIFTS spectra, XPS spectra, EXAFS spectra, XANES spectra, soot-TPO, *in-situ* NO oxidation DRIFTS spectra, and DFT calculations) is available in the online version of this article at https://doi.org/10.26599/NR.2025.94907431.

Data availability

All data needed to support the conclusions in the paper are presented in the manuscript and the Electronic Supplementary Material. Additional data related to this paper may be requested from the corresponding author upon request.

Acknowledgements

We acknowledge the financial support from the National Key Research and Development Program of China (No. 2022YFB3504100), the National Natural Science Foundation of China (Nos. 22376217, 22208373, 22272106, and 12305372), and Key Laboratory of Jiangxi Province for Persistent Pollutants Prevention Control and Resource Reuse (No. 2023SSY02061). The authors wish to thank the facility support of the beamlines BL13SSW at SSRF.

Declaration of competing interest

All the contributing authors report no conflict of interests in this work.

Author contribution statement

Y. F. L. and T. Q.: Data curation, validation, writing manuscript, experimental design. H. G., L. S. X., Y. X. M., B. L. C., J. X. and P. Z.: Data curation. Y. C. W., X. L., Y. P. L., L. W. C., J. L., and Z. Z.: Data curation, project administration, funding acquisition. All the authors have approved the final manuscript.

Use of AI statement

None.

References

[1] Zhang, P.; Chen, T. Z.; Ma, Q. X.; Chu, B. W.; Wang, Y. H.; Mu, Y. J.; Yu, Y. B.; He, H. Diesel soot photooxidation enhances the heterogeneous formation of H_2SO_4. *Nat. Commun.* **2022**, *13*, 5364.

[2] Mei, X. Y.; Zhu, X. B.; Zhang, Y. X.; Zhang, Z. L.; Zhong, Z. C.; Xin, Y.; Zhang, J. Decreasing the catalytic ignition temperature of diesel soot using electrified conductive oxide catalysts. *Nat. Catal.* **2021**, *4*, 1002–1011.

[3] Weng, R. X.; Mei, X. Y.; Zhang, Z. L.; Xin, Y.; Xu, J. Q.; Zhang, Y. X.; Zhang, J. Affecting factors of electrified soot combustion on potassium-supported antimony tin oxides. *Chem. Eng. J.* **2023**, *465*, 143046.

[4] Peng, C.; Ren, Y.; Yu, D.; Wang, L. Y.; Zhang, C. L.; Fan, X. Q.; Yu, X. H.; Zhao, Z.; Wei, Y. C.; Liu, J. K-modified MnO_δ catalysts with tunnel structure and layered structure: Facile preparation and catalytic performance for soot combustion. *Nano Res.* **2023**, *16*, 6187–6199.

[5] Andana, T.; Piumetti, M.; Bensaid, S.; Veyre, L.; Thieuleux, C.; Russo, N.; Fino, D.; Quadrelli, E. A.; Pirone, R. Nanostructured equimolar ceria-praseodymia for NO_x-assisted soot oxidation: Insight into Pr dominance over Pt nanoparticles and metal–support interaction. *Appl. Catal. B: Environ.* **2018**, *226*, 147–161.

[6] Legutko, P.; Stelmachowski, P.; Yu, X. H.; Zhao, Z.; Sojka, Z.; Kotarba, A. Catalytic soot combustion-general concepts and alkali promotion. *ACS Catal.* **2023**, *13*, 3395–3418.

[7] Wang, M.; Zhang, Y.; Yu, Y. B.; Shan, W. P.; He, H. Cesium as a dual function promoter in Co/Ce-Sn catalyst for soot oxidation. *Appl. Catal. B: Environ.* **2021**, *285*, 119850.

[8] Oi-Uchisawa, J.; Wang, S. D.; Nanba, T.; Ohi, A.; Obuchi, A. Improvement of Pt catalyst for soot oxidation using mixed oxide as a support. *Appl. Catal. B: Environ.* **2003**, *44*, 207–215.

[9] Li, Y. F.; Qin, T.; Wei, Y. C.; Xiong, J.; Zhang, P.; Lai, K. Z.; Chi, H. J.; Liu, X.; Chen, L. W.; Yu, X. L. et al. A single site ruthenium catalyst for robust soot oxidation without platinum or palladium. *Nat. Commun.* **2023**, *14*, 7149.

[10] Zhang, Q. L.; Li, G.; Liu, W. M.; Li, G. B.; He, T. Y.; Zhang, H. X.; Yu, Y. B.; Peng, H. G. Constructing highly active zeolite encapsulated PdAg alloy catalysts for typical VOCs deep oxidation: The role of electron–structure interaction. *Appl. Catal. B Environ. Energy* **2024**, *352*, 124051.

[11] Kong, J. J.; Tang, M. Q.; Luo, Y. J.; Song, S. N.; Xiang, Z. W.; Guo, Y. L.; Zhang, W. P.; Li, G. Y.; An, T. C. Pyroelectric Pt-supported S-scheme heterojunction catalyst for effective photocatalytic degradation of VOCs containing soot driven by visible light. *Appl. Catal. B Environ. Energy* **2025**, *365*, 124858.

[12] Yu, D.; Peng, C.; Ren, Y.; Wang, L. Y.; Zhang, C. L.; Fan, X. Q.; Yu, X. H.; Zhao, Z. Low temperature oxidation of diesel soot particles over one-dimensional 2 × 3 tunnel-structured $Na_2Mn_5O_{10}$ catalysts. *Appl. Catal. B Environ. Energy* **2024**, *344*, 123614.

[13] Chen, L. W.; Zhang, J.; Wang, J.; Chen, P. R.; Fu, M. L.; Wu, J. L.; Ye, D. Q. Insight into the improvement effect of nitrogen dopant in Ag/Co_3O_4 nanocubes for soot oxidation: Experimental and theoretical studies. *J. Hazard. Mater.* **2021**, *420*, 126604.

[14] Li, X.; Pereira-Hernández, X. I.; Chen, Y. Z.; Xu, J.; Zhao, J. K.; Pao, C. W.; Fang, C. Y.; Zeng, J.; Wang, Y.; Gates, B. C. et al. Functional CeO_x nanoglues for robust atomically dispersed catalysts. *Nature* **2022**, *611*, 284–288.

[15] Li, X. N.; Yang, X. F.; Huang, Y. Q.; Zhang, T.; Liu, B. Supported noble-metal single atoms for heterogeneous catalysis. *Adv. Mater.* **2019**, *31*, 1902031.
[16] Yu, D.; Yu, X. H.; Zhang, C. L.; Wang, L. Y.; Fan, X. Q.; Zhao, Z.; Wei, Y. C.; Liu, J.; Gryboś, J.; Leszczyński, B. et al. Layered $Na_2Mn_3O_7$ decorated by Cerium as the robust catalysts for efficient low temperature soot combustion. *Appl. Catal. B Environ.* **2023**, *338*, 123022.
[17] Frank, B.; Schlögl, R.; Su, D. S. Diesel soot toxification. *Environ. Sci. Technol.* **2013**, *47*, 3026–3027.
[18] Sellers-Antón, B.; Bailón-García, E.; Cardenas-Arenas, A.; Davó-Quiñonero, A.; Lozano-Castelló, D.; Bueno-López, A. Enhancement of the generation and transfer of active oxygen in Ni/CeO_2 catalysts for soot combustion by controlling the Ni-ceria contact and the three-dimensional structure. *Environ. Sci. Technol.* **2020**, *54*, 2439–2447.
[19] Wang, N.; Sun, Q. M.; Bai, R. S.; Li, X.; Guo, G. Q.; Yu, J. H. *In situ* confinement of ultrasmall Pd clusters within nanosized silicalite-1 zeolite for highly efficient catalysis of hydrogen generation. *J. Am. Chem. Soc.* **2016**, *138*, 7484–7487.
[20] Sun, Y. W.; Xu, G. Y.; Wang, Y. J.; Shi, W.; Yu, Y. B.; He, H. *In situ* synthesis of encapsulated Pd@silicalite-2 for highly stable methane catalytic combustion. *Environ. Sci. Technol.* **2023**, *57*, 20370–20379.
[21] Liu, Y. W.; Li, Z.; Yu, Q. Y.; Chen, Y. F.; Chai, Z. W.; Zhao, G. F.; Liu, S. J.; Cheong, W. C.; Pan, Y.; Zhang, Q. H. et al. A general strategy for fabricating isolated single metal atomic site catalysts in Y zeolite. *J. Am. Chem. Soc.* **2019**, *141*, 9305–9311.
[22] Pham, T. C. T.; Kim, H. S.; Yoon, K. B. Growth of uniformly oriented silica MFI and BEA zeolite films on substrates. *Science* **2011**, *334*, 1533–1538.
[23] Xie, L. J.; Liu, F. D.; Liu, K.; Shi, X. Y.; He, H. Inhibitory effect of NO_2 on the selective catalytic reduction of NO_x with NH_3 over one-pot-synthesized Cu-SSZ-13 catalyst. *Catal. Sci. Technol.* **2014**, *4*, 1104–1110.
[24] Andana, T.; Piumetti, M.; Bensaid, S.; Veyre, L.; Thieuleux, C.; Russo, N.; Fino, D.; Quadrelli, E. A.; Pirone, R. Ceria-supported small Pt and Pt_3Sn nanoparticles for NO_x-assisted soot oxidation. *Appl. Catal. B Environ.* **2017**, *209*, 295–310.
[25] Andana, T.; Piumetti, M.; Bensaid, S.; Veyre, L.; Thieuleux, C.; Russo, N.; Fino, D.; Quadrelli, E. A.; Pirone, R. CuO nanoparticles supported by ceria for NO_x-assisted soot oxidation: Insight into catalytic activity and sintering. *Appl. Catal. B Environ.* **2017**, *216*, 41–58.
[26] Liu, S.; Wu, X. D.; Luo, H.; Weng, D.; Ran, R. Pt/zeolite catalysts for soot oxidation: Influence of hydrothermal aging. *J. Phys. Chem. C* **2015**, *119*, 17218–17227.
[27] Liu, S.; Wu, X. D.; Weng, D.; Li, M.; Ran, R. Roles of acid sites on Pt/H-ZSM5 catalyst in catalytic oxidation of diesel soot. *ACS Catal.* **2015**, *5*, 909–919.
[28] Zhou, X. X.; Zhang, H.; Sun, Y. Y.; Gao, Z.; Chen, H. R. Defective zeolite TS-1 confined Pt nanoclusters with superior performance for CO and soot catalytic oxidation. *Fuel* **2023**, *351*, 128805.
[29] He, T. Y.; Li, G. B.; Ji, J.; Liu, W. M.; Zhang, H. X.; Xie, X. Q.; Huang, S.; Huang, T.; Peng, H. G. Tailored engineering of intracrystalline mesopores for boosting multicomponent volatile organic compounds simultaneous deep oxidation. *Appl. Catal. B Environ. Energy* **2025**, *362*, 124752.
[30] Cao, X. Q.; Zhou, J.; Li, S.; Qin, G. W. Ultra-stable metal nano-catalyst synthesis strategy: A perspective. *Rare Met.* **2020**, *39*, 113–130.
[31] Sun, Q. M.; Wang, N.; Zhang, T. J.; Bai, R. S.; Mayoral, A.; Zhang, P.; Zhang, Q. H.; Terasaki, O.; Yu, J. H. Zeolite-encaged single-atom rhodium catalysts: Highly-efficient hydrogen generation and shape-selective tandem hydrogenation of nitroarenes. *Angew. Chem., Int. Ed.* **2019**, *58*, 18570–18576.
[32] Wu, S. M.; Yang, X. Y.; Janiak, C. Confinement effects in zeolite-confined noble metals. *Angew. Chem., Int. Ed.* **2019**, *58*, 12340–12354.
[33] Zhu, C. F.; Li, W. Y.; Chen, T. X.; He, Z.; Villalobos, E.; Marini, C.; Zhou, J.; Woon Lo, B. T.; Xiao, H.; Liu, L. C. Boosting the stability of subnanometer Pt catalysts by the presence of framework indium(III) sites in zeolite. *Angew. Chem., Int. Ed.* **2024**, *63*, e202409784.
[34] Li, J. L.; Zhang, Q.; He, G. Y.; Zhang, T. J.; Li, L.; Li, J. Y.; Hao, D. P.; Zhang, W.; Terasaki, O.; Mei, D. H. et al. Silanol-stabilized atomically dispersed $Pt^{\delta+}$–O_x–Sn active sites in protozeolite for propane dehydrogenation. *J. Am. Chem. Soc.* **2024**, *146*, 24358–24367.
[35] Zhang, Q.; Gao, S. Q.; Yu, J. H. Metal sites in zeolites: Synthesis, characterization, and catalysis. *Chem. Rev.* **2023**, *123*, 6039–6106.
[36] Liu, Y.; Chen, Y.; Gao, Z. R.; Zhang, X.; Zhang, L. J.; Wang, M.; Chen, B. B.; Diao, Y. N.; Li, Y. L.; Xiao, D. Q. et al. Embedding high loading and uniform Ni nanoparticles into silicalite-1 zeolite for dry reforming of methane. *Appl. Catal. B Environ. Energy* **2022**, *307*, 121202.
[37] Kresse, G.; Furthmüller, J. Efficient iterative schemes for *ab initio* total-energy calculations using a plane-wave basis set. *Phys. Rev. B* **1996**, *54*, 11169–11186.
[38] Blöchl, P. E. Projector augmented-wave method. *Phys. Rev. B* **1994**, *50*, 17953–17979.
[39] Song, S. J.; Yang, K.; Zhang, P.; Wu, Z. J.; Li, J.; Su, H.; Dai, S.; Xu, C. M.; Li, Z. X.; Liu, J. et al. Silicalite-1 stabilizes Zn-hydride species for efficient propane dehydrogenation. *ACS Catal.* **2022**, *12*, 5997–6006.
[40] Wei, G. L.; Zhou, L. S.; Luo, J. H.; Yu, B.; Ding, F. Y.; Song, J. F.; Shi, Y.; Zhang, J. Q.; Feng, X. W.; Liu, N. Insight into the catalytic oxidation mechanism of hydrogen isotopes by Pt clusters confined by silicalite-1. *Inorg. Chem.* **2024**, *63*, 14171–14182.
[41] Meng, X. L.; Wang, C. Z.; Chae, S.; Wang, Y. J.; Wu, C.; Xi, S. B.; Catizzone, E.; Giordano, G.; Guo, H. L.; Mintova, S. $CuZnO_x$ active sites anchored on the silanols of hollow silicalite-1 zeolite enhance CO_2 hydrogenation to methanol. *ACS Catal.* **2025**, *15*, 5412–5425.
[42] Teranishi, T.; Hosoe, M.; Tanaka, T.; Miyake, M. Size control of monodispersed Pt nanoparticles and their 2D organization by electrophoretic deposition. *J. Phys. Chem. B* **1999**, *103*, 3818–3827.
[43] Cheng, W. D.; Zhao, M. Y.; Lai, Y. C.; Wang, X.; Liu, H. Y.; Xiao, P.; Mo, G.; Liu, B.; Liu, Y. P. Recent advances in battery characterization using *in situ* XAFS, SAXS, XRD, and their combining techniques: From single scale to multiscale structure detection. *Exploration* **2024**, *4*, 20230056.
[44] Wu, L. K.; Deng, J. G.; Liu, Y. X.; Jing, L.; Yu, X. H.; Tao, J. X.; Gao, R. Y.; Feng, Y.; Dai, H. X. Enhanced removal efficiency of multicomponent VOCs over the Sn-doped silicalite-1-supported Ru single-atom catalysts by constructing tightly coupled redox and acidic sites. *Appl. Catal. B Environ. Energy* **2024**, *351*, 123910.
[45] Luo, Y. J.; Serrano-Lotina, A.; Budihardjo, F. F.; Taghipour, S.; Ferdousi, S. A.; Li, L. P.; Delgado, J. J.; López-Buendía, Á.; Portela, R.; Han, W. et al. Photoactive nano-confined Pt in titania nanotubes (Pt-TiNT) via microwave-assisted flow synthesis. *Chem. Eng. J.* **2023**, *466*, 143254.
[46] Dong, J. S.; Zhang, Y. T.; Li, D. K.; Adogwa, A.; Huang, S. J.; Yang, M.; Yang, J. Q.; Jin, Q. Q. Reaction-driven evolutions of Pt states over $Pt\text{-}CeO_2$ catalysts during CO oxidation. *Appl. Catal. B Environ.* **2023**, *330*, 122662.
[47] Tan, W.; Cai, Y. D.; Yu, H. W.; Xie, S. H.; Wang, M. Y.; Ye, K. L.; Ma, L.; Ehrlich, S. N.; Gao, F.; Dong, L. et al. Tuning the interaction between platinum single atoms and ceria by zirconia doping for efficient catalytic ammonia oxidation. *Environ. Sci. Technol.* **2023**, *57*, 15747–15758.
[48] Zhang, R.; Wang, X.; Wang, K.; Wang, H. L.; Liu, L.; Wu, X. T.; Geng, B. K.; Chu, X.; Song, S. Y.; Zhang, H. J. Synergism of ultrasmall Pt clusters and basic $La_2O_2CO_3$ supports boosts the reverse water gas reaction efficiency. *Adv. Energy Mater.* **2023**, *13*, 2203806.
[49] Di, M. Q.; Simmance, K.; Schaefer, A.; Feng, Y. Y.; Hemmingsson,

F.; Skoglundh, M.; Bell, T.; Thompsett, D.; Ajakaiye Jensen, L. I.; Blomberg, S. et al. Chasing PtO_x species in ceria supported platinum during CO oxidation extinction with correlative *operando* spectroscopic techniques. *J. Catal.* **2022**, *409*, 1–11.

[50] Yang, W. W.; Li, M. Y.; Zhang, B. K.; Liu, Y. Z.; Zi, J. Z.; Xiao, H.; Liu, X. Y.; Lin, J. K.; Zhang, H. Y.; Chen, J. et al. Interfacial microenvironment modulation boosts efficient hydrogen evolution reaction in neutral and alkaline. *Adv. Funct. Mater.* **2023**, *33*, 2304852.

[51] You, Y.; Han, P. J.; Song, S.; Luo, W.; Zhao, S. N.; Han, K. J.; Tian, Y.; Yan, N.; Li, X. G. Distinct selectivity control in solar-driven bio-based α-hydroxyl acid conversion: A comparison of Pt nanoparticles and atomically dispersed Pt on CdS. *Angew. Chem., Int. Ed.* **2023**, *62*, e202306452.

[52] Li, L.; Luo, H.; Shao, Z. L.; Zhou, H. Z.; Lu, J. W.; Chen, J. J.; Huang, C. J.; Zhang, S. N.; Liu, X. F.; Xia, L. et al. Converting plastic wastes to naphtha for closing the plastic loop. *J. Am. Chem. Soc.* **2023**, *145*, 1847–1854.

[53] Lee, J.; Christopher, P. Does H_2 temperature-programmed reduction always probe solid-state redox chemistry. *The case of Pt/CeO_2. Angew. Chem., Int. Ed.* **2025**, *64*, e202414388.

[54] He, L. J.; Zhang, Y.; Zang, Y. C.; Liu, C. X.; Wang, W. C.; Han, R.; Ji, N.; Zhang, S. T.; Liu, Q. L. Promotion of A-site Ag-doped perovskites for the catalytic oxidation of soot: Synergistic catalytic effect of dual active sites. *ACS Catal.* **2021**, *11*, 14224–14236.

[55] Wei, X. E.; Cheng, J. W.; Li, Y. B.; Cheng, K.; Sun, F. F.; Zhang, Q. H.; Wang, Y. Bimetallic clusters confined inside silicalite-1 for stable propane dehydrogenation. *Nano Res.* **2023**, *16*, 10881–10889.

[56] Xuan, C. B.; Han, S. W.; Wang, L. Y.; Zhang, X. Y.; Sun, R. F.; Cheng, X. X.; Wang, Z. Q.; Ma, C. Y.; Zhao, T. T.; Hou, X. K. Mechanism of NO reduction by NH_3 over $CuMnO_x$ catalysts and the influence mechanism of CO. *Catal. Sci. Technol.* **2023**, *13*, 3106–3124.

[57] Shen, T.; Shi, X. K.; Guo, J. X.; Li, J.; Yuan, S. D. Photocatalytic removal of NO by light-driven Mn_3O_4/BiOCl heterojunction photocatalyst: Optimization and mechanism. *Chem. Eng. J.* **2021**, *408*, 128014.

[58] Liu, L. J.; Zheng, X. T.; Su, S.; Yu, J. Y.; Liu, T.; Wang, Y.; Hu, S.; Xiang, J. Efficient MnFeW/Ti catalyst for simultaneous removal of NO and Hg^0 in flue gas at low temperature: Effect of NO on Hg^0 oxidation and reaction mechanism. *Fuel* **2022**, *327*, 125218.

[59] Mosrati, J.; Atia, H.; Eckelt, R.; Huyen Vuong, T.; Rabeah, J.; Mhamdi, M.; Armbruster, U. Ta and Mo oxides supported on CeO_2-TiO_2 for the selective catalytic reduction of NO_x with NH_3 at low temperature. *J. Catal.* **2021**, *395*, 325–339.

[60] Wang, Z. Y.; Wei, Q. H.; Zhang, N.; Shi, X. J.; Chen, M. J.; Huang, Y.; Cao, J. J.; Li, H. W.; Ho, W.; Lee, S. Simultaneous polarization engineering and selectivity regulation achieved using polymeric carbon nitride for promoting NO_x photo-oxidation. *Appl. Catal. B Environ.* **2023**, *330*, 122582.

[61] Ye, L.; Lu, P.; Yan, X. H.; Huang, H. B. Boosting simultaneous catalytic removal of NO_x and toluene via cooperation of Lewis acid and oxygen vacancies. *Appl. Catal. B Environ.* **2023**, *331*, 122696.

[62] Fang, D.; He, F.; Liu, X. Q.; Qi, K.; Xie, J. L.; Li, F. X.; Yu, C. Q. Low temperature NH_3-SCR of NO over an unexpected Mn-based catalyst: Promotional effect of Mg doping. *Appl. Surf. Sci.* **2018**, *427*, 45–55.